INORGANIC CHEMISTRY FRONTIERS

RESEARCH ARTICLE

View Article Online
View Journal | View Issue

Cite this: *Inorg. Chem. Front.*, 2024, **11**, 5725

Metal centers and aromatic moieties in Schiff base complexes: impact on G-quadruplex stabilization and oncogene downregulation†

Aurane Froux, [a,b] Luisa D'Anna, [a] Aurianne Rainot, [a,c] Camille Neybecker, [b] Angelo Spinello, [a] Riccardo Bonsignore, [a] Raphaël Rouget, [b] Guillaume Harlé, [b] Alessio Terenzi, [a] Antonio Monari, [c] Stéphanie Grandemange *[b] and Giampaolo Barone *[a]

Received 3rd June 2024,
Accepted 13th July 2024

DOI: 10.1039/d4qi01394h

rsc.li/frontiers-inorganic

We present the synthesis and characterization of novel square planar transition metal complexes of Schiff base ligands, which act as guanine quadruplex binders and stabilizers. The complexes stabilize quadruplexes related to telomere stability or present in oncogene regulatory sequences, as determined by optical spectroscopy, pointing out the emergence of selectivity towards specific structures or sequences. These results are supported and rationalized by molecular modeling simulations. Furthermore, we show that the treatment of cancer cell lines with our complexes is associated with the increase in the number of nuclear guanine quadruplexes and the downregulation in the expression of the considered oncogenes. Remarkably, only very moderate cytotoxicity can be observed for all complexes. These results pave the way for the development of selective anticancer treatment by metal compounds targeting the expression of specific oncogenes.

Introduction

Guanine quadruplexes (G4) are nowadays recognized as fundamental nucleic acid motifs with important regulatory and protective functions in cells.[1] As such, their deregulation has also been linked to the emergence of debilitating and life-threatening diseases, including cancer and neurodegenerative disorders.[2–4] Their presence in the genome of microorganisms such as viruses and bacteria has also been recently pointed out.[5–8] G4s could represent ideal pharmacological targets to finely tune and regulate cellular responses.[4,9] Yet, the widespread use of G4-targeting drugs is still hampered by a general lack of selectivity, which may correlate with increased, and in some cases heavy, secondary effects. Clearly the rational design of drugs aimed at controlling the G4 cellular level will greatly benefit from a deeper understanding of the structural interplay between the nucleic acids and the chosen drugs. Indeed, from a structural point of view, G4s share a common rigid core, constituted by a superposition of tetramers composed of four guanines stabilized by Hoogsten hydrogen bond patterns.[1,10] The G4 superstructure is also highly dependent on π-stacking interactions and shows the concomitant presence of a rigid core and flexible backbone and loop units. The flexibility of the loops and the possible orientation of the glycosidic bond also lead to the well-known G4 polymorphisms reflected in the presence of parallel, antiparallel, and hybrid structures.[9,10]

G4 structures can form in both RNA and DNA sequences and may arise from single or multiple nucleic acid strands.[1] However, single-stranded DNA-based G4s are by far the more commonly encountered, as also shown by the larger number of solved structures. They are found in guanine-rich regions of the genome, and different bioinformatic tools exist to predict their presence from the analysis of a given sequence.[11–13] In eukaryotic cells the presence of G4s is particularly important in telomeres, where they play a protective role on the chromosome ends, and in non-coding gene expression regions, where they may be seen as regulatory check-points.[14] Indeed, telomere G4 stabilization, impeding their unfolding, is effective at inhibiting telomerase activity, thus preventing the emergence of immortality phenotypes in cancer cells.[4] G4s have also been found in several oncogene promoters, such as *kRAS*, *BCL2*, or *cMYC*, which are all importantly involved in different steps of carcinogenesis.[15–17] However, the G4 regulatory role in gene-expression is highly complex. While G4 stabilization is usually related to a downregulation of gene expression,[18–21] in some

[a]*Università di Palermo, Department of Biological, Chemical and Pharmaceutical Sciences and Technologies Viale delle Scienze, Edificio 17, 90128 Palermo, Italy. E-mail: giampaolo.barone@unipa.it*
[b]*Université de Lorraine, CNRS, CRAN, F-54000 Nancy, France. E-mail: stephanie.grandemange@univ-lorraine.fr*
[c]*Université Paris Cité and CNRS, ITODYS, F-75006 Paris, France*
† Electronic supplementary information (ESI) available. See DOI: https://doi.org/10.1039/d4qi01394h

cases G4 may recruit transcription factors that lead to upregulation of their expression.[9,22] Furthermore, in some crucial oncogene promoting regions, such as *c-KIT*, multiple G4s exist in close spatial proximity, giving rise to a strong coupling, which may even influence their individual topology and biological role.[23,24]

Despite these difficulties, the development of G4 stabilizers is still considered a promising therapeutic strategy, and indeed some G4-targeting drugs have reached the clinical test stage.[25,26] Effective stabilizers need to show a strong G4-binding selectivity compared to their propensity toward double-helical DNA (B-DNA), to avoid global genomic instability.[27] Furthermore, a preferential selectivity for only a limited number of G4 sequences, presenting a peculiar structure and topology, would be desirable.

Given the global structural features of G4s, square planar metal complexes are among the motifs of choice in the design of G4 stabilizers.[14,28,29] Indeed, the presence of extended π-conjugated systems allows for a favourable end-stacking with the G4 tetrads, while minimizing the competitive intercalation into DNA structures. Furthermore, peripheral positive charges are clearly beneficial in increasing water solubility and in favouring the stabilization of the G4/ligand aggregate by developing electrostatic stabilization with the nucleic acid backbone phosphate groups. Different complexes of transition metal ions have been proposed as suitable G4 stabilizers[30] which have been largely tested on DNA[31–36] and RNA oligomers, as well as *in vitro*.[26] As for the ligand counterpart, salphen moieties have proven their efficacy in providing an ideal π-stacking scaffold and, most importantly, in increasing their selectivity *versus* G4 compared to B-DNA.[14,32,34,37]

However, the effects of the extension of the ligand π-conjugation on the G4 binding and selectivity might be explored in more depth, together with the fine role of the positively charged substituents in improving the electrostatic stabilization. Motivated by these considerations, we present a systematic study on square planar transition metal complexes of Schiff bases as G4 binders. In particular, we assess the binding selectivity towards different relevant G4 sequences present in human oncogenes and telomeres. Furthermore, we also examine the often-overlooked role of the central metal ion in promoting G4 binding and selectivity towards a specific sequence. Finally, we also show that G4 stabilization nicely correlates with the downregulation of the corresponding specific oncogene, even when cytotoxic effects are rather limited. Therefore, our results provide a general framework for the development of G4-oriented therapies specifically targeting the expression of selected oncogenes, thus reducing systemic toxicity and side effects of chemotherapeutic approaches.

Results and discussion

Synthesis and characterization

Salphen-like metal complexes have already proven their efficiency in promoting selective binding to G4 structures. Here, we have focused on improving their potentiality by acting on two structural/electronic factors, namely: (i) the introduction of a 4-methyl-pyridinium group to bring peripheral positive charges on the chelating ligand and maximize electrostatic interactions with the DNA backbone, and (ii) varying the extension of the π-conjugated system on the N–N bridge, tuning the π-stacking with the G4 quartets. The main proposed compounds together with their synthetic routes are presented in Scheme 1. Note that our proposed modifications of the aldehyde moiety have led to the development of an extensive and modulable library of potential ligands, all bearing two formally positive charges on the lateral substituents. To enlarge the chemical space of our potential G4 binders we have, indeed, considered complexation with different metal ions, namely Zn(II), Ni(II), Cu(II), Pd(II), and Pt(II) (Scheme 1). Furthermore, the obtained compounds were grouped based on the extension of the π-conjugated substituents belonging to the salen, salphen and salnaphen families, respectively.

An efficient synthetic route was devised to allow the production of our extensive library of compounds. To this aim, 5-chloromethylsalicylaldehyde was functionalized with 4-methylpyridine, *via* a nucleophilic substitution reaction conducted in the tetrahydrofuran solvent, yielding the positively charged pyridinium **B** (Scheme 1), which represents the fundamental building block for obtaining the whole library of metal complexes.

The final compounds, belonging to the class of Schiff base metal complexes, have been obtained by template synthesis, during which **B** is condensed, in the presence of the given metal salt, with three different diamines: *o*-phenylenediamine to give the salphen family, ethylenediamine to provide the salen family, and 2,6-naphthalenediamine to afford the salnaphen family.

Metal complexes **1–12** were obtained in a one-step reaction, without previous isolation of the ligand, based on similar reported procedures.[38–41] Indeed, aldehyde **B** was directly con-

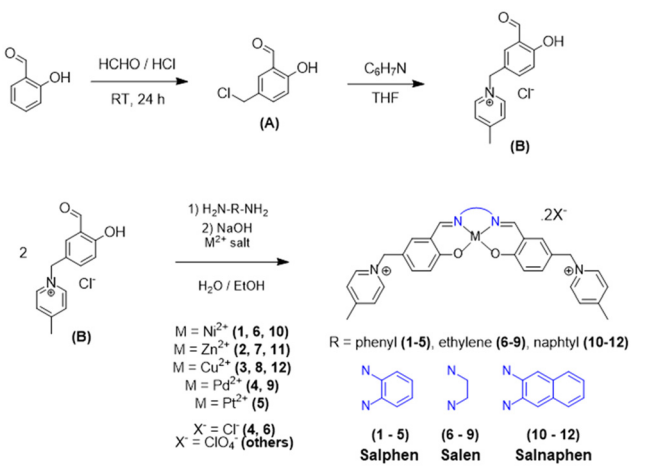

Scheme 1 Reaction pathways for the synthesis of compound **B** and complexes **1–12**.

densed with the chosen primary diamine to obtain the Schiff base ligand, which was deprotonated with a strong base, before coordination with the corresponding metal salt (Scheme 1). The explicit structure of each complex is listed in Fig. S1.†

For the synthesis and purification of the Pt(II) complex **5**, we opted for a successive precipitation and counterion exchange strategy as described in the Experimental section. The chloride salt was firstly exchanged with sodium hexafluorophosphate. The final Pt(II) product was obtained after ion exchange with the Amberlite Cl-form resin, to give the Pt (II) complex **5** as a chloride salt. While this strategy induced a reduction of the global reaction yield, it significantly improved the purity of the final product. The salen Pt(II) and salnaphen Pd(II) and Pt(II) complexes were not obtained with the required purity and were discarded for this study.

Intermediate **B** and complexes **1–12** have been characterized by ^{1}H-NMR spectroscopy (Fig. S2†), except for the paramagnetic copper(II) complexes, as well as mass spectrometry (Fig. S3†) and elemental analysis (Experimental section). Concerning the NMR signals of the symmetric metal complexes, each peak obviously corresponds to double the number of protons, as specified in the labelling schemes presented in each spectrum of Fig. S2.†

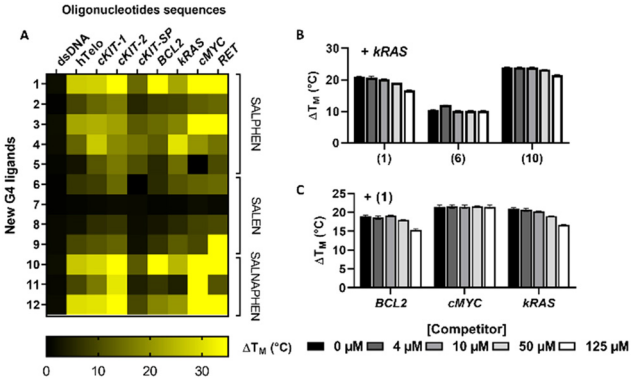

Fig. 1 (A) Heatmap of the stabilizing behaviour of the 12 metal complexes on the selected G4-folded oligonucleotides obtained by the FRET melting curve assay. The darkest region corresponds to the absence of stabilization and the brightest yellow to the highest induced stabilization ΔT_M (°C). (B) Stabilization of *kRAS* G4 by the three Ni(II) compounds **1** (salphen), **6** (salen) and **10** (salnaphen), in the presence of increasing concentrations of duplex DNA competitor (ctDNA). (C) Stabilizing ability of compound **1** towards *BCL2*, *cMYC* and *kRAS* G4, in the presence of increasing concentrations of the ctDNA competitor. DNA was dissolved in 0.2 μM solutions, in the presence of 1 μM of the metal complex, in 60 mM or 10 mM potassium cacodylate buffer at pH 7.4.

DNA-binding in solution

The binding strength of our metal complexes towards different G4 sequences, adopting different topologies, has been investigated using Förster Resonance Energy Transfer (FRET) melting assays. In addition, the selectivity towards G4 was also assessed by comparing the affinity of our complexes for either G4s or for a self-complementary double-stranded DNA (dsDNA) mimicking the double-helical B-DNA conformation. The chosen G4 sequences correspond to a variety of biologically relevant G4 motifs, including the human telomers (hTelo)[42,43] and oncogene promoters *BCL2*,[44] *kRAS*,[45] *cMYC*,[46] and *RET*.[47] Furthermore, the three G4 units present in the whole *cKIT*[24,48] sequence have been used. The sequences of all G4s used are listed in Table S1.†

To assess G4 stabilization, we labelled each oligomer with a FRET active fluorophore and monitored the changes in the melting temperature (T_M) after the addition of our complexes in a ratio of 1 : 5 [DNA] : [metal complex]. An increase in T_M reveals stabilization induced by complex binding.

The data in Fig. 1A summarize the changes in the melting temperature (ΔT_M) of each DNA sequence bound to the corresponding metal complex (see also Table S2† for the numerical values of ΔT_M). Importantly, none of the 12 compounds presented significant stabilization of dsDNA, while a statistically significant increase in the melting temperature was observed for the G4s. As of note, and mainly in the presence of compounds **1**, **3**, **10** and **12** the stabilization achieved using a 1 : 5 ratio was so strong that the instrumental maximum of ΔT_M = 30 °C was exceeded. This is particularly noticeable for compound **10** interacting with *cKit2*, *BCL2*, *cMYC*, and *RET* G4s.

Some additional global tendencies can also be extracted from our data. The salen family members (**6–9**) appear as the weakest G4 stabilizers both in term of melting temperature increase and of the number of targeted G4 which are stabilized. Conversely, the salnaphen group (**10–12**) clearly outstands the other families in promoting the strongest G4 stabilization. This result is not surprising and clearly highlights the beneficial role of the extended conjugation pattern in promoting favourable interactions with the guanine tetrads.

Ni(II) metal complexes (complexes **1**, **6** and **10**) appear to be the most efficient G4 stabilizers compared to other analogues. This fact is particularly evident when comparing compound **1** to the isostructural Pd(II) and Pt(II) compounds **4** and **5**, indicating the important role of the metal centre. Interestingly, the affinity trend obtained by FRET measurements of salphen complexes **1**, **4** and **5**, decreases with the increase of the atomic number of group 10 elements, in the order Ni > Pd > Pt. The stronger affinity of Ni compound **1**, compared to the analogous Pd and Pt compounds **4** and **5**, could be attributed to the higher positive charge on the center of the metal complex, determined by the higher ionic character of the Ni–N and Ni–O bonds, compared to that of the analogous Pd/Pt–N and Pd/Pt–O bonds, being characterized by a higher covalent nature.[49]

Finally, while neither specificity nor selectivity toward a particular G4 sequence emerged unambiguously from our study, our results suggest a preference of the metal complexes for parallel topologies. Indeed, parallel G4 sequences (*BCL2*, *kRAS*, *c-MYC*, *RET* and *c-KIT2*) are stabilized by most of the metal complexes. Conversely, the anti-parallel *c-KIT-SP* (Fig. 1A) is the least stabilized sequence.

Thus, these results clearly show that our metal compounds, particularly **1**, **3**, **10** and **12**, may be classified as potentially strong G4 stabilizers.

To better assess their selectivity, we have evaluated the specificity of some G4 stabilizers with *kRAS* sequence *versus* dsDNA. To this aim, FRET melting assays were performed in the presence of increasing concentrations of the unlabelled B-DNA competitor (calf thymus DNA, ctDNA) and Ni(II) complexes **1**, **6** and **10**. As indicated in Fig. 1B, even in the presence of both G4 and dsDNA, the three compounds induce a strong and specific stabilization of the *kRAS* G4. Indeed, at the maximum concentration of dsDNA, complex **1** showed a reduction of the stabilization capability towards G4 of around 20%. The other complexes were even less affected by the presence of the competitor DNA. Indeed, complex **10** presents a reduction of stabilization amounting to 10%, while remarkably, the stabilization potential of complex **6** was almost unaffected and has been reduced by only 2%. The specificity of **1** for different G4 structures, namely, *BCL2*, *cMYC*, and *kRAS*, has been deeply analysed. A competitive FRET assay showed a reduction of about 20% of the stabilization of *BCL2* and *kRAS* G4s in the presence of 125 μM dsDNA (Fig. 1C). Interestingly, cMYC G4 was very strongly stabilized by complex **1** at an initial ratio of 1 : 5, with the consequence that just a minor increase in FAM fluorescence was observed when the temperature is increased (see Fig. S4†). This exceptional stabilization did not allow us to determine the G4 melting temperature upon interaction with complex **1** under these experimental conditions. For this reason, the compound concentration was reduced from 1.0 to 0.60 μM to reach a [G4 DNA]/[complex **1**] of 1 : 3. Even under these conditions, no reduction of *cMYC* G4 stabilization was observed also at a higher concentration of double helical DNA (<0.2%).

We have also investigated the G4 binding ability of compounds **1**, **6** and **10** by UV-vis and circular dichroism (CD) spectroscopy, using again ctDNA as a comparison.

For the binding studies, two different double-stranded DNA sequences were used: UV-vis and CD experiments were performed using calf-thymus DNA, while FRET experiments were conducted in the presence of dsDNA, a self-complementary 20-mer oligonucleotide bearing a central linker (see Table S1†). Despite this difference, both sequences adopt the same conformation and display the same spectral signals.[50]

The evolution of DNA topologies upon increasing the amounts of metal complexes was monitored by circular dichroism measurements. After checking the correct folding of the parallel quadruplexes *kRAS*, *BCL2* and *cMYC* by the negative and positive ellipticities at 240 and 260 nm, respectively, we evaluated how increasing amounts of **1**, **6** and **10** would perturb such patterns. As shown in Fig. 2, the addition of **1** and **10** led to a general hypochromic effect at 260 nm in all the G4 spectra. This is coherent with significant binding, and so confirms the FRET experiment. Interestingly, CD spectra of ctDNA were strongly modified by the addition of compounds **1** and **10** (Fig. 2A and E). A strong interaction is suggested by the consequent hyperchromic shift of the 270 nm band for both compounds **1** and **10**. Notably, the increase of **1** corresponds to an induced positive band at 366 nm and a negative one at 306 nm, while **10** caused the appearance of a positive band around 360 nm and the accentuation of the ctDNA negative one at 250 nm. Such results suggest, on the one hand, that the topology of the G4 is globally maintained, since no major changes are observed in the CD spectra. On the other hand, the changes in the ctDNA CD spectrum are probably connected with the presence of a CD band induced by the metal complexes and/or with a stronger alteration of the DNA structure. Finally, compound **6** did not yield significant changes in the CD spectra of ctDNA or G4s (Fig. S5†). The lack of spectral changes of the Ni(II) salen complex **6** suggests that an external binding mode, different from intercalation, is occurring here. On the other hand, the perturbation of the CD spectra of ctDNA shown in Fig. 2A and E, in the presence of salphen and

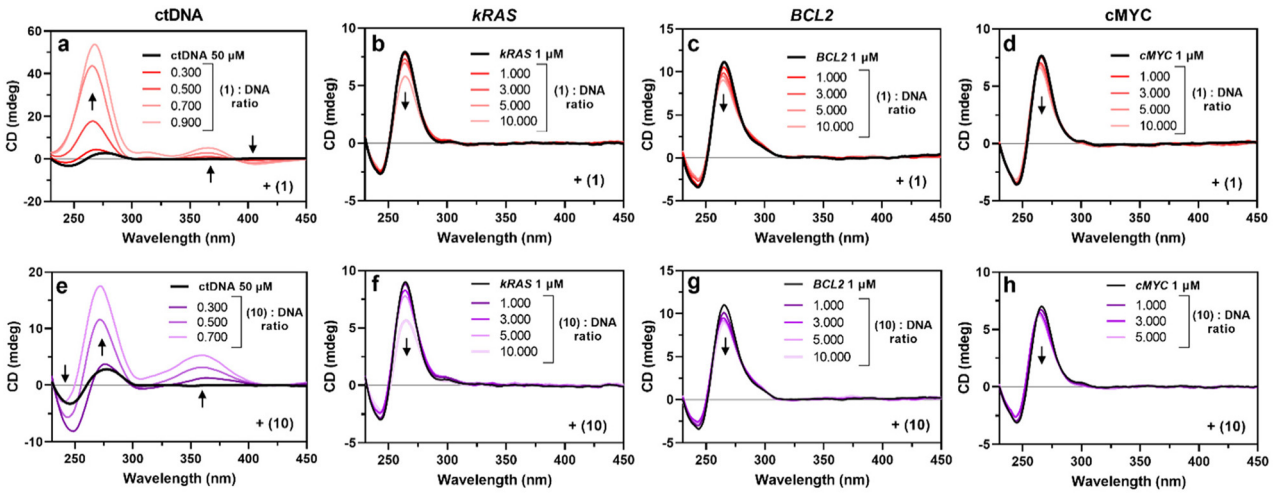

Fig. 2 Compounds **1** and **10** strongly interact with DNA. Circular dichroism spectra of ctDNA (a and e), *kRAS* (b and f), *BCL2* (c and g) and *cMYC* (d and h) with increasing concentrations of complex **1** (a–d) or complex **10** (e–h), in 50 mM Tris HCl, 100 mM KCl, pH 7.4.

salnaphen Ni(II) complexes **1** and **10**, points out the occurrence of consistent structural modification of the double helix DNA after intercalation. The strong DNA binding of compounds **1** and **10** is also witnessed by the appearance of induced CD bands at around 300 and 450 nm, respectively.

The characterization of the G4 binding ability of Ni(II) compounds **1**, **6** and **10** was extended by determining their intrinsic DNA-binding constants (K_b), by titrating each complex with increasing amounts of nucleic acid. We monitored the UV-vis spectra of the corresponding complex in the 300–400 nm region, where the complex exhibits a characteristic absorption band (**1**: 366 nm; **6**: 316 nm; **10**: 350 nm) and where none of the investigated oligomers absorb (Fig. S6–S8†). Intrinsic binding constants could be determined by applying the Thordarson equation and are listed in Table 1.[51] The three tested compounds present higher K_b values with ctDNA than G4 structures. The high K_b values obtained from ctDNA titration are consistent with the important changes in the ctDNA CD spectra. Importantly, the absence of stable double helix stabilization observed in the FRET assay does not necessarily indicate a lack of interaction.

Moreover, the small binding constants obtained by the UV-vis titration of G4 sequences consistently correlate with the poor hypochromism observed for the CD spectra of the titrated G4. It is worth pointing out that the significant stabilization of G4 induced by our compounds, as shown by FRET experiments, does not align with the value of the binding constants obtained by UV-Vis and the impact on the CD signals of the used sequences. While a perfect agreement among the three methods, FRET, UV-vis, and CD, used to characterize intermolecular interactions would be ideal, such coherence may be unrealistic due to the intrinsic differences in the experimental approaches. Specifically, the significant increase in ΔT_M observed in FRET experiments may arise from interactions that do not markedly alter the conformation of G4s, and therefore do not significantly impact their CD spectra. This phenomenon can be primarily attributed to system stabilization *via* external electrostatic attraction between the negative phosphate groups and the positive charges of the metal compounds, rather than specific non-covalent interactions like π–π stacking. In contrast, the pronounced changes in the CD spectra of ctDNA upon interaction with compounds 1 and 10 (Fig. 2A and E) suggest that these compounds intercalate ctDNA, leading to substantial conformational changes such as base stacking disruption. Such structural modification does not occur after the interaction of our metal complexes with G4s, which possess a rigid core as also evidenced by MD simulations (*vide infra*). This clearly points to the occurrence of a top-stacking binding mode with the drug candidate overhanging on the peripheral tetrad.

Table 1 Intrinsic binding constants for Ni(II) compounds **1**, **6** and **10** with different DNA topologies. K_b (M^{-1}) values were determined by the UV-vis titration of the compound with increasing concentrations of DNA in 50 mM Tris-HCl and 100 mM KCl, pH 7.5

	Binding constant K_B (M^{-1})		
	1	**6**	**10**
ctDNA	$(3.83 \pm 0.06) \times 10^4$	$(1.68 \pm 0.06) \times 10^4$	$(1.17 \pm 0.06) \times 10^5$
kRAS	$(5.89 \pm 0.12) \times 10^3$	$(5.74 \pm 0.16) \times 10^3$	$(4.79 \pm 0.05) \times 10^3$
BCL2	$(2.40 \pm 0.02) \times 10^2$	$(3.89 \pm 0.02) \times 10^3$	$(7.67 \pm 0.06) \times 10^3$
cMYC	$(4.25 \pm 0.17) \times 10^4$	$(1.37 \pm 0.02) \times 10^4$	$(7.78 \pm 0.15) \times 10^3$

In silico characterization

To better understand the binding capacity of the different transition metal complexes towards G4s, we have performed all-atom molecular dynamics simulation to study the interaction of Ni-salphen (**1**) and Ni-salnaphen (**10**) complexes with *kRAS* and *BCL2*'s G4s, respectively.

As shown in Fig. 3 and 4 the formation of a stable complex maintained by favourable π-stacking and electrostatic interactions is observed in the early stage of the unbiased MD simulation and maintained during the entire μs time-span, especially for the interaction with *kRAS*. This can be most notably observed by the time evolution of the root mean

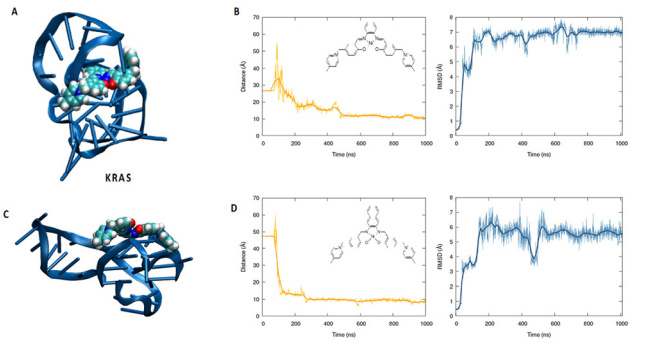

Fig. 3 Representative snapshot of the interaction between Ni-salphen compound **1** (A) and Ni-salnaphen compound **10** (C) complex and the *kRAS*' G4 as obtained by MD simulations. The corresponding time evolution of the RMSD and of the distance between the centres of mass of the G4 and the complex are reported in panel (B) and (D), respectively.

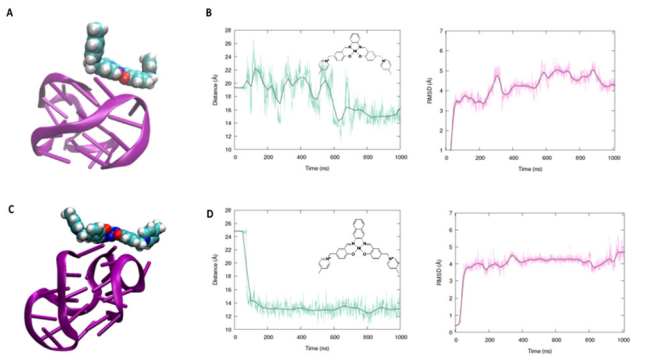

Fig. 4 Representative snapshot of the interaction between Ni-salphen **1** (A) and Ni-salnaphen **10** (C) complex and the *BCL2*'s G4 as obtained by MD simulations. The corresponding time evolution of the RMSD and of the distance between the centres of mass of the G4 and the complex are reported in panel (B) and (D), respectively.

square deviation (RMSD) and of the distance between the centre of mass of the transition metal and the G4. Interestingly, as it can be also observed from the representative snapshot reported in Fig. 3, the interaction with the transition metal complex involves the interaction with both the tetrads and the G4 loops. This behaviour seems particularly important for the interaction with *BCL2*'s *G4*. Indeed, a rather large structural reorganization taking place in the 500 ns range is observed for this structure while interacting with the salphen complex (**1**). This is also coherent with the lower binding constant experimentally determined. In the case of the salnaphen system, while a persistent aggregate is observed, the latter is not forming an optimal π-stacking with the tetrad (Fig. 4) and is, instead, opportunistically interacting with the extruded loop bases, suggesting a less pronounced stabilization of the G4. Conversely, for both G4s the interaction with the ligand does not induce any important structural deformation of the G4 and is only partially affecting the dynamics of the flexible loop present in the *kRAS* oncogene, in coherence with the CD spectra. Interestingly, interactions with the loops are also favourable for maintaining the aggregate as shown in Fig. 3. Globally, MD simulations confirm that the stabilization of *kRAS*'s G4 by our transition metal complexes is more favourable than for its *BCL2* counterpart. This is coherent with the experimental observations and is most probably due to the fact that *kRAS*'s G4 allows a more optimal stacking scaffold to accommodate large and rigid metal complexes.

G4 stabilization in cells

Encouraged by the promising results obtained in solution and *in silico*, we have investigated the effect of G4 stabilization in cells. Notably, the ability of compounds **1**, **6** and **10** to affect the G4 landscape in cancer cell lines was assessed by the immunocytofluorescence assay. We hypothesize that our compounds should induce an increase in the number of cellular G4s. Thus, pancreatic cancer T3M4 cells were treated with increasing concentrations of compounds **1**, **6** or **10**, as shown in Fig. 5. Nuclear G4 foci were counted and the median number of foci for each condition was compared with the control, which was treated with the DMSO vehicle. While compound **1** affected G4 numbers solely at 50 μM, compounds **6** and **10** had more important effects. The counted nuclear foci increased with the concentration of the metal complex, revealing a dose-dependent response of the G4 presence in cells treated with compounds **6** and **10**. Particularly, compound **10** provoked a strong increase in the nuclear G4 numbers at 5 μM, as compared to the control (Fig. 5). Thus, our results suggest that these compounds are efficient at shaping the amount of G4, and thus the genome landscape in cancer cells. Furthermore, these results confirm that our complexes induce G4 stabilization in a cellular environment, coherent with the *in vitro* results.

Oncogene expression regulation

Since we have achieved the stabilization of G4 sequences involved in the modulation of gene expression, we investigated

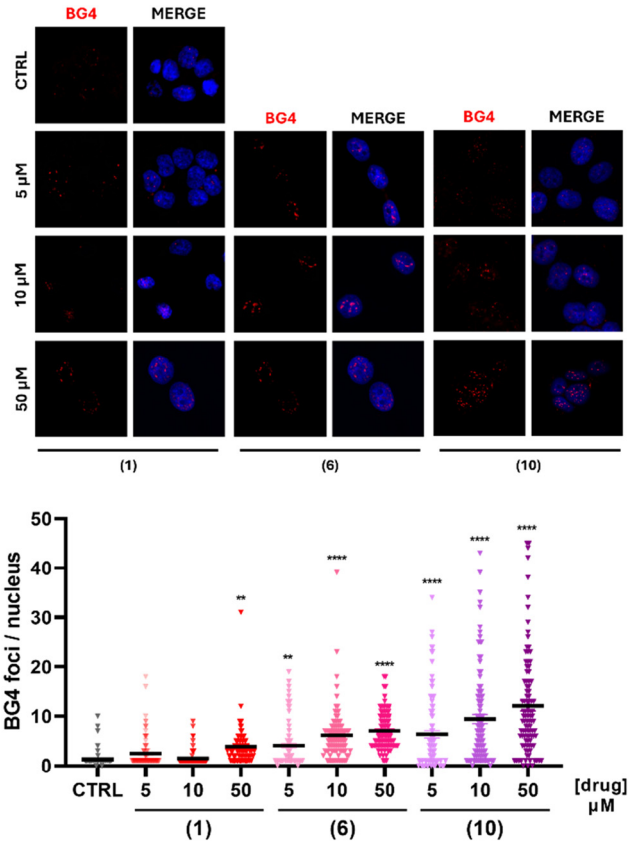

Fig. 5 Immunodetection of nuclear G4 in cancerous cells and the impact of G4 stabilizers. T3M4 cells were treated for 24 hours with 5, 10 or 50 μM of compound **1**, **6** or **10**. Nuclear G4s were detected by immunocytofluorescence, using BG4 antibodies (red channel). Nuclear BG4 foci were enumerated considering 100 cells. Mean ± SEM. (n = 3); **p < 0.01; ***p < 0.001; ****p < 0.0001. One-way ANOVA.

if the transcription level of the studied *kRAS*, *cMYC*, *BCL2*, and *RET* oncogenes was altered in the presence of our compounds.

While *kRAS* and *cMYC* expression levels were evaluated using T3M4 cells, *BCL2* and *RET* were quantified on T47D cells, according to the basal gene expression level, specific to each cell line previously investigated (data not shown). The cells were treated for 6 hours with 50 μM of each complex, and the transcript level was assessed by RT-qPCR. The results are expressed relative to the control (Fig. 6). A downregulation of the *kRAS* transcript level is significantly observed after the treatment of the cells with 6 of the 12 complexes (Fig. 6A). However, the Zn(II) compounds, especially **2** and **11**, showed a strong reduction in *kRAS* expression by around 3-fold. In T3M4 cells, *cMYC* was also downregulated, notably by compounds **1**, **2**, **5**, **10** and **11** by about 1.4-fold and even more strongly by compound **12**, which resulted in a 1.9-fold reduction (Fig. 6A).

Conversely, *BCL2* transcripts were downregulated only by complex **5** (Fig. 6B) with a fold-change of approximately 1.6 and were globally unaltered by the other compounds. Finally, *RET* was more affected compared to the other transcripts since 8 of the 12 complexes led to its downregulation by around 2-fold (Fig. 6B).

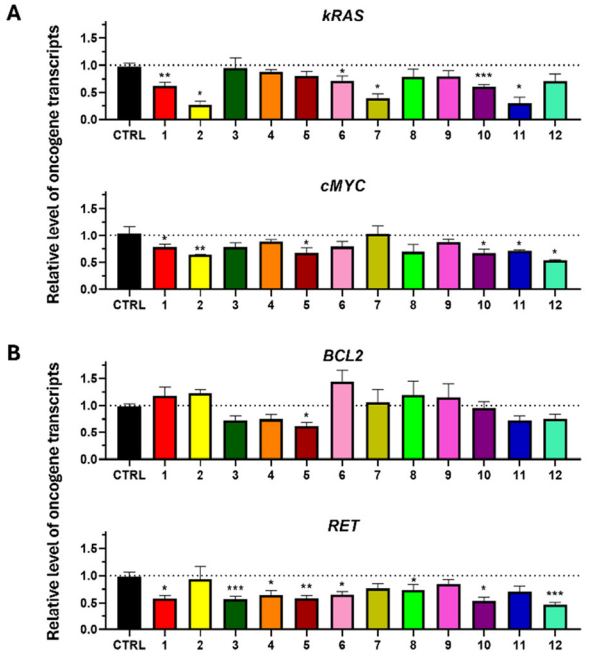

Fig. 6 The expression level of the considered oncogene was evaluated by RT-qPCR after treating cells for 6 hours with 50 μM of the corresponding compound. (A) *kRAS* and *cMYC* transcript levels were evaluated on T3M4 cells, while *BCL2* and *RET* (B) were assessed on T47D cells. Data are shown as expression level, relative to the control conditions (reported for **1**). For representation, the control (CTRL) is the mean of different controls. Significance for each treated condition is expressed compared to its internal control. Mean ± SEM. (n = 4) t-test.

If these results do not correlate perfectly with the G4 stabilization pattern observed in solution (Fig. 1A), they confirm the global trend. Namely they confirm that our complexes can stabilize the G4 folding, and thus, modulate the expression level of the investigated oncogenes, mostly leading to their significant downregulation.

We tested the expression of a large range of G4s contained in oncogene promoters and demonstrated the ability of our complexes to strongly stabilize them. The list of the oncogene expression evaluation is larger than those generally found in the literature and highlights their capacity to efficiently downregulate a wide panel of G4-driven oncogenes. No real specificity towards a particular oncogene has been observed (except for *BCL2* being downregulated solely by compound **5**), but a kind of parallel conformation preference emerges. If those results are at a previous stage in the characterization of the oncogene modulator capacity of those new compounds, major efforts could be made for a deeper and larger identification of the gene targets, through RNA sequencing analysis after treating the cells with some G4 stabilizers. This approach would allow a strong characterization and identification of the molecular targets under G4 landscape modulation.

Effect on cell viability and proliferation

The observed stabilization of G4 and the inhibition of oncogene expression by our metal complexes led us to determine their impact on cell viability and proliferation in aggressive cancer models. Indeed, kRAS, RET and cMYC proteins play key roles in regulating cell proliferation and the anti-apoptotic protein BCL2 is particularly involved in cell survival.[15,27,52–54]

Cell viability after treatment with the G4 stabilizers **1–12** has been evaluated on three different human cancer cell lines, derived from human pancreatic ductal adenocarcinoma (T3M4), triple-negative (MDA-MB-231) and hormone-dependent (T47D) breast ductal carcinoma. The half maximal inhibitory concentration (IC_{50}) of the 12 complexes was determined after 48 hours of incubation, by exposing the cells to a range of concentrations spanning 1 to 200 μM (Fig. 7A and S9–S11†). For some complexes (*e.g.* **2** on MDA-MB-231 cells), the inhibition of 50% of the cellular population was not reached under such conditions (Fig. S11†). Therefore, the concentration of 50 μM for a duration of 48 hours was chosen to determine the viability of the three cell lines. The majority of our compounds significantly reduced the viability of the three cell lines tested (Fig. 7B–D). However, MDA-MB-231 cells appeared less sensitive to the treatment compared to T3M4 and T47D cells. As a matter of fact, 5 complexes (**2**, **3**, **6**, **9** and **11**) showed IC_{50} values higher than 200 μM for MDA-MB-231 cells, while only one (**9**) for T3M4 and none for T47D cells. This difference could be associated with the lower cell line doubling time of the MDA-MB-231 cell line (44 ± 4.6 hours) compared with T3M4 (20 ± 0.5 hours) and T47D (30 ± 1.3 hours) models (Fig. S12†). Indeed, it is widely reported that G4 formation is dependent of cell cycle dynamics. G4 struc-

A

	IC_{50} at 48 hours (μM)		
	T3M4	T47D	MDA-MB-231
1	26.0 ± 3.1	64.1 ± 2.3	68.7 ± 4.5
2	52.0 ± 4.4	40.3 ± 5.9	> 200
3	17.4 ± 6.5	92.6 ± 17.1	> 200
4	142.9 ± 11.1	70.6 ± 5.0	166.3 ± 47.4
5	38.2 ± 3.3	34.8 ± 4.6	39.7 ± 11.1
6	69.6 ± 28.6	125.7 ± 8.9	> 200
7	53.4 ± 8.1	59.6 ± 5.9	> 200
8	42.3 ± 8.2	86.1 ± 13.5	90.4 ± 5.2
9	> 200	135.1 ± 16.3	> 200
10	81.7 ± 15.9	64.9 ± 9.1	94.2 ± 29.0
11	107.6 ± 31.6	35.9 ± 5.0	> 200
12	50.8 ± 15.5	75.7 ± 12.9	184.9 ± 38.7

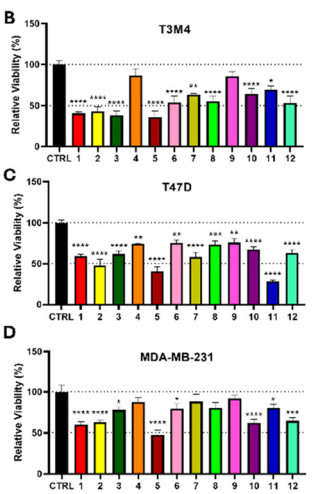

Fig. 7 Half maximal inhibitory concentration IC_{50} determination on T3M4, MDA-MB-231 and T47D cell lines. (A) IC_{50} of the **12** compounds on T3M4, T47D and MDA-MB-231 cell models at 48 hours of treatment, determined by the crystal violet assay. Mean ± SEM (n = 5). Relative viability of pancreatic cancer cells T3M4 (B), hormonal-dependent breast cancer cells T47D (C) and triple-negative breast cancer cells MDA-MB-231 (D) upon treatment with 50 μM of the corresponding compound for 48 hours, determined by crystal violet (n = 4). Mean ± SEM; *p < 0.05; **p < 0.01; ***p < 0.001; ****p < 0.0001. One-way ANOVA.

tures are described to preferentially form during the S phase, due to the replication fork.[55,56]

The results obtained point out that most of the 12 compounds have strong stabilizing effects in solution, except for zinc(II) compound **7**. In the cellular environment, the stabilizing activity was confirmed by the analysis of oncogene expression, pointing out that only compound **9** does not repress gene expression on any of the four tested oncogenes. To confirm these results, we have chosen three compounds to analyze by immunocytofluorescence their impact on the number of G4 foci in cells. As indicated in Fig. 5, while the increase of the G4 foci is more relevant with compound **10** than with compound **1**, the three nickel(II) compounds **1**, **6** and **10** show significant stabilizing activities for G4 structures in a cellular environment. Thus, although in solution data indicate strong stabilization activity of most of compounds, it appears that in a cellular context the binding/stabilizing activity of complexes can be different because of their entry into the cells and/or the nucleus. However, the use of a large variety of experiments in solution and in cells, allowed us to highlight the compounds with the most relevant activity.

Furthermore, the real time proliferation rate of the treated cancer cells with increasing concentrations (0, 1, 10 and 50 μM) of our metal complexes was followed for 72 hours. Ni(II) compounds **1**, **6** and **10** showed a strong antiproliferative capacity at 50 μM (Fig. 8), generally after 48 hours of treatment. No dose-dependent response was observed between 10 and 50 μM. Interestingly, some complexes showed complete inhibition of cell proliferation over the time-span, such as **1** on T3M4 (Fig. 8A) and T47D (Fig. 8B), suggesting a total arrest of the cell cycle. The proliferation inhibition rate at 48 and 72 hours of the other complexes is reported in Table S3.† Globally, we may conclude that while our G4 stabilizers affect the proliferation and viability of all the three tested cancer cell line models, they were poorly cytotoxic as underlined by the need to use high doses (approx. 50 μM) to induce a significant proliferation inhibition.

Those effects at 50 μM over time are in perfect coherence with the ones obtained from the evaluation of oncogene expression (Fig. 6). Indeed, compounds **1**, **6** and **10** significantly downregulate *kRAS*, *cMYC* and *RET* oncogenes, and are known as the key regulators of cell proliferation.[27,52]

On the other hand, our results on T3M4 cells treated with compound **1** suggest a total arrest in the cell cycle progression. Further experiments and analysis of the cell cycle should be performed to characterize these results.

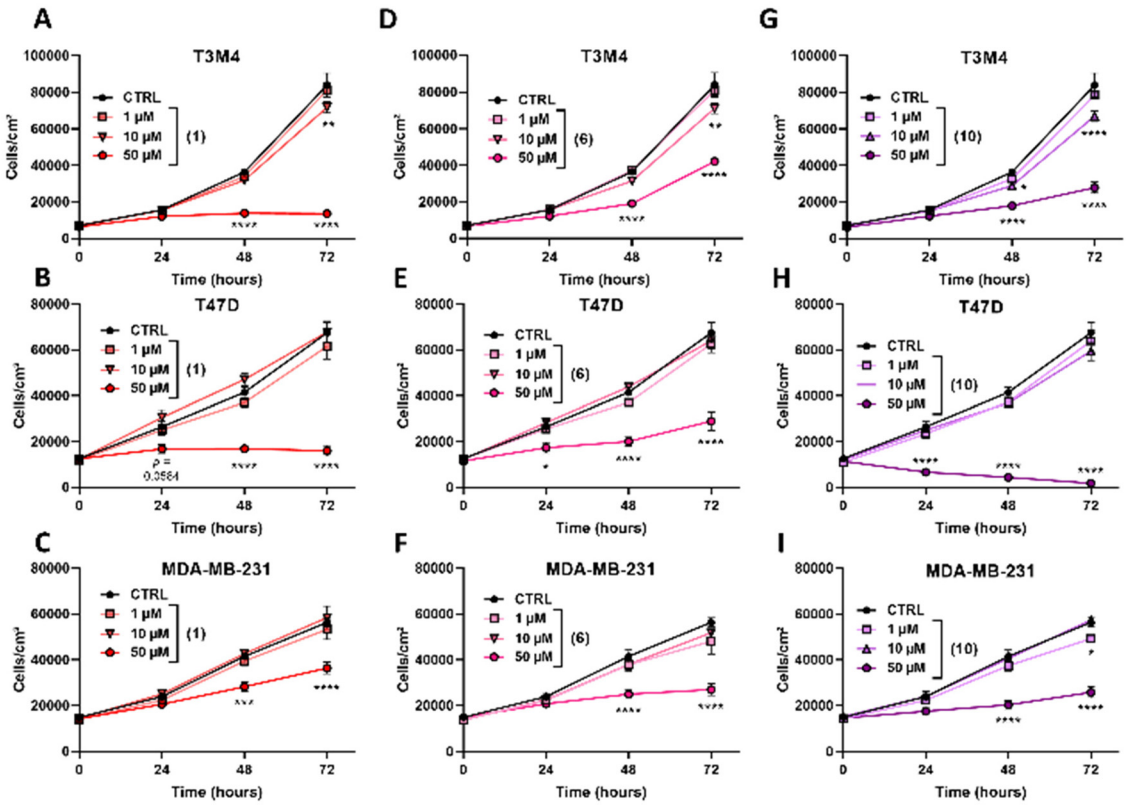

Fig. 8 The proliferation of T3M4 (upper panel), T47D (middle panel) and MDA-MB-231 (lower panel) cell lines was followed by the real-time cell imager Cytonote (IPRASENSE®), over 72 hours while treated with different concentrations of nickel(II) compounds **1** (A–C), **6** (D–F) and **10** (G–I). Mean ± SEM (n = 3); *p < 0.05; **p < 0.01; ***p < 0.001; ****p < 0.0001. Two-way ANOVA.

Experimental section

Synthetic procedures

General. Commercial grade chemicals and solvents were purchased from Sigma Aldrich and Thermo Fisher Scientific, and used without further purification. ^{1}H and ^{13}C NMR spectra were recorded on Bruker AC-E series 300 MHz, while elemental analyses were performed using an Eurovector EA3000 elemental analyzer at the Microanalytical Laboratory of the University of Vienna and the University of Lorraine, laboratory L2CM. Mass spectrometry experiments were carried out on an Agilent 6540 QTOF LC/MS.

5-Chloromethylsalicylaldehyde (A). The starting material 5-chloromethylsalicylaldehyde (**A**) was synthesized as previously described.[40,57] Briefly, 5 mL of salicylaldehyde was added to 14.4 mL of formaldehyde and 50 mL of conc. HCl for 24 hours at room temperature. The resulting precipitate was filtered and washed with abundant *n*-hexane.

5-(4-Methylpyridin-1-ium)-salicylaldehyde chloride (B). 5-(4-Methylpyridin-1-ium)-salicylaldehyde chloride ($C_{14}H_{14}ClNO_2$) (**B**) was obtained by the dropwise addition of 4-methylpyridine (486.6 μL; 5 mmol) to a solution of 5-chloromethylsalicyladehyde (**A**) (852.9 mg; 5 mmol) in tetrahydrofuran. The mixture was mixed at room temperature until the complete consumption of both reactants. The resulting white solid was recovered by filtration and washed with cold diethyl ether (922.6 mg; 70% yield). ^{1}H NMR (400 MHz, DMSO-d_6) δ 11.15 (s, 1H), 10.28 (s, 1H), 9.06–9.00 (d, 2H), 7.98 (d, J = 6.4 Hz, 2H), 7.85 (d, J = 2.4 Hz, 1H), 7.69 (dd, J = 8.6, 2.5 Hz, 1H), 7.11 (d, J = 8.6 Hz, 1H), 5.72 (s, 2H), 2.59 (s, 3H). ESI-MS (*m*/*z*). Calculated for $C_{14}H_{14}NO_2$ $[2M + Cl]^+$ 491.17; found 491.17.

Synthesis of Schiff base metal complexes. Metal complexes were synthesized in a one pot reaction, without previous isolation of the ligand. The general method for the synthesis of the salphen metal compounds (**1**, **2**, and **3**) is described above. The prepared compound **B**, (263.8 mg; 1 mmol) was dissolved in H_2O/EtOH 1 : 1 (5 mL), and solid NaOH (40.0 mg; 1 mmol) was added before stirring at room-temperature for 20 minutes. Parallelly, an aqueous solution of 1,2-phenylenediamine (54.1 mg; 0.5 mmol) was prepared with $M(ClO_4)_2{\cdot}6H_2O$ (0.55 mmol) (with M = Ni, Zn or Cu) and dropwise added to the first solution. The resulting mixture was left stirring at room-temperature for 4 hours. The obtained precipitate was filtered under reduced pressure and washed with cold water, ethanol and diethyl ether. Salen metal compounds (**6**, **7**, and **8**) were synthesized as the salphen compounds, but pure ethylenediamine (33.4 μL; 0.5 mmol) was added instead of 1,2-phenylenediamine. Salnaphen compounds (**10**, **11**, and **12**) were obtained as the salphen complexes but *o*-phenylenediamine was replaced with 2,6-naphthalenediamine (79.2 mg; 0.5 mmol). The obtained salnaphen solids were recrystallized in a solution of acetonitrile, acetone and water 1 : 2 : 3 to obtain the final compounds.

Salphen Ni(II) complex (1). Red precipitate (272.7 mg; 69.5% yield). ^{1}H NMR (400 MHz, DMSO-d_6) δ 9.36 (s, 1H), 9.00–8.94 (m, 2H), 8.12 (dt, J = 7.1, 3.6 Hz, 1H), 8.01 (d, J = 6.4 Hz, 2H), 7.70 (d, J = 2.4 Hz, 1H), 7.46 (dd, J = 8.9, 2.4 Hz, 1H), 7.41 (dt, J = 6.3, 3.6 Hz, 1H), 6.94 (d, J = 8.9 Hz, 1H), 5.69 (s, 2H), 2.61 (s, 3H). Elemental analysis of $C_{34}H_{30}Cl_2N_4O_{10}Ni{\cdot}3.5H_2O$ (**1**). Calculated: C 48.20%; H 4.40%; N 6.61%. Found: C 48.07%; H 4.05%; N 6.70%. ESI-MS (*m*/*z*). Calculated for $(C_{34}H_{30}N_4O_2Ni)_2(ClO_4)_2$ $[M]^{2+}$ 684.12; found 684.12.

Salphen Zn(II) complex (2). Yellowish precipitate (279.9 mg; 70.8% yield). ^{1}H NMR (300 MHz, DMSO-d_6) δ 8.99 (s, 1H), 8.96 (d, J = 3.2 Hz, 2H), 7.99 (d, J = 6.3 Hz, 2H), 7.86 (dt, J = 8.4, 4.1 Hz, 1H), 7.58 (d, J = 2.5 Hz, 1H), 7.43 (dd, J = 6.0, 3.3 Hz, 1H), 7.38 (dd, J = 8.8, 2.4 Hz, 1H), 6.73 (d, J = 8.8 Hz, 1H), 5.63 (s, 2H), 2.60 (s, 3H). Elemental analysis of $C_{34}H_{30}Cl_2N_4O_{10}Zn{\cdot}1.5H_2O$ (**2**). Calculated: C 49.93%; H 4.07%; N 6.85%. Found: C 49.84%; H 3.96%; N 7.01%. ESI-MS (*m*/*z*). Calculated for $(C_{34}H_{30}N_4O_2Zn)_2(ClO_4)_2$ $[M]^{2+}$ 691.11; found 691.11.

Salphen Cu(II) complex (3). Dark green solid (262.6 mg; 66.6% yield). Elemental analysis of $C_{34}H_{30}Cl_2N_4O_{10}Cu{\cdot}3.5H_2O$ (**3**). Calculated: C 48.20%; H 4.40%; N 6.61%. Found: C 48.07%; H 4.05%; N 6.70%. ESI-MS (*m*/*z*). Calculated for $(C_{34}H_{30}N_4O_2Cu)_2(ClO_4)_2$ $[M]^{2+}$ 689.11; found 689.12. The elemental analysis of compound **3** shows that two of the three elements have a tolerance deviation higher than ±0.40% of the calculated values.[58]

Salphen Pd(II) complex (4). A solution of compound **B** (132 mg; 0.5 mmol) was stirred at room temperature in the presence of 1,2-phenylenediamine (27.1 mg; 0.25 mmol) for 30 minutes, before adding an aqueous solution of Pd $(CH_3CO_2)_2$ (62.0 mg; 0.275 mmol). The mixture was allowed to react at room temperature for 2 hours. To this, $NaClO_4{\cdot}6H_2O$ (40.0 mg; 0.275 mmol) was added and stirred for 2 hours at room temperature. The resulting orange solid was recovered by filtration. The product was re-suspended in water and placed in the Amberlite® IRA-402 Cl form ion exchange resin (Thermo Fisher Scientific). The reaction was allowed to stir at room temperature for 24 hours, under a nitrogen atmosphere. The day after, the resin was washed with abundant cold H_2O, and cold EtOH. A brownish solution was recovered by filtration, and the solvent was evaporated by lyophilization. A strongly orange product was recovered (66.6 mg; 37.9% yield). ^{1}H NMR (400 MHz, DMSO-d_6) δ 9.20 (s, 1H), 9.00 (dd, J = 6.0, 4.3 Hz, 2H), 8.34 (dd, J = 6.4, 3.4 Hz, 1H), 8.01 (dd, J = 6.6, 4.9 Hz, 2H), 7.86 (d, J = 2.5 Hz, 1H), 7.57 (dd, J = 8.9, 2.4 Hz, 1H), 7.50 (dd, J = 6.3, 3.3 Hz, 1H), 7.07 (d, J = 8.9 Hz, 1H), 5.73 (s, 2H), 3.29 (s, 3H). Elemental analysis of $C_{34}H_{30}Cl_2N_4O_{10}Pd{\cdot}5H_2O$ (**4**). Calculated: C 51.43%; H 5.08%; N 7.06%. Found: C 51.19%; H 4.76%; N 7.79%. ESI-MS (*m*/*z*). Calculated for $(C_{34}H_{30}N_4O_2Pd)_2(ClO_4)_2$ $[M]^{2+}$ 732.09; found 732.09.

Salphen Pt(II) complex (5). Compound **B** (105.5 mg; 0.4 mmol) was dissolved in H_2O and NaOH (16.0 mg; 0.4 mmol) was added under a nitrogen atmosphere at room temperature for 20 minutes. The entire reaction was performed with nitrogen bubbling directly in the solution. The pH was adjusted to 7.4 with conc. HCl. 1,2-Phenylenediamine (21.7 mg; 0.2 mmol) was added to the previous solution, and

the mixture was allowed to stir at room temperature, for 30 min. K_2PtCl_4 (83.5 mg; 0.2 mmol) was added to the solution, and left stirring at room temperature for 4 hours. The resulting reddish precipitate was filtered under reduced pressure and washed with cold water. The product (79.1 mg; 0.1 mmol) was then resuspended in H_2O/EtOH 1 : 1 (30 mL), and $NaPF_6$ (67.2 mg; 0.4 mmol) was added to the solution. The mixture was stirred at room-temperature, under an inert atmosphere for 2 hours, before adding the same quantity of $NaPF_6$ and allowed to react for 24 hours. The resulting solid was harvested by filtration and washed with abundant cold water and diethyl ether. The red powder was then exchanged with Amberlite® IRA-402 Cl form ion exchange resin (Thermo Fisher Scientific) in water, under an inert atmosphere for 24 hours. The day after, the resin was washed with abundant cold water and ethanol. The solvents were eliminated by lyophilization. A reddish powder was recovered (37.6 mg; 47.4% yield). ^{1}H NMR (400 MHz, DMSO-d_6) δ 9.55 (s, 1H), 9.04 (d, J = 6.1 Hz, 2H), 8.56–8.34 (m, 1H), 8.02 (d, J = 6.7 Hz, 3H), 7.70 (dd, J = 9.0, 2.2 Hz, 1H), 7.48 (dd, J = 6.4, 3.2 Hz, 1H), 7.16 (d, J = 8.9 Hz, 1H), 5.79 (s, 2H), 2.62 (s, 3H). Elemental analysis of $C_{34}H_{30}Cl_2N_4O_{10}Pt{\cdot}8H_2O$ (**5**). Calculated: C 43.60%; H 4.95%; N 5.98%. Found: C 43.57%; H 4.58%; N 6.53%. ESI-MS (m/z). Calculated for $(C_{34}H_{30}N_4O_2Pt)_2(Cl)_2$ $[M]^{2+}$ 757.17; found 757.17.

Salen Ni(II) complex (6). Red solid (164.4 mg; 45% yield). ^{1}H NMR (400 MHz, DMSO-d_6) δ 8.94 (d, J = 6.3 Hz, 2H), 7.97 (d, J = 6.2 Hz, 2H), 7.89 (s, 1H), 7.46 (d, J = 2.5 Hz, 1H), 7.32 (dd, J = 8.8, 2.4 Hz, 1H), 6.74 (d, J = 8.8 Hz, 1H), 5.60 (s, 2H), 3.45 (s, 2H), 2.59 (s, 3H). Elemental analysis of $C_{30}H_{30}Cl_2N_4O_{10}Ni{\cdot}3H_2O$ (**6**). Calculated: C 45.60%; H 4.59%; N 7.09%. Found: C 45.76%; H 4.67%; N 7.43%. ESI-MS (m/z). Calculated for $(C_{30}H_{30}N_4O_2Ni)_2(ClO_4)_2$ $[M]^{2+}$ 636.12; found 636.12.

Salen Zn(II) complex (7). Light orange precipitate (135.6 mg; 36.5% yield). ^{1}H NMR (300 MHz, DMSO-d_6) δ 9.01–8.92 (d, 2H), 8.40 (s, 1H), 7.97 (d, J = 6.3 Hz, 2H), 7.38 (d, J = 2.6 Hz, 1H), 7.29 (dd, J = 8.8, 2.6 Hz, 1H), 6.64 (d, J = 8.7 Hz, 1H), 5.57 (s, 2H), 3.73 (s, 2H), 2.58 (s, 3H). Elemental analysis of $C_{30}H_{30}Cl_2N_4O_{10}Zn{\cdot}4H_2O$ (**7**). Calculated: C 44.22%; H 4.70%; N 6.88%. Found: C 44.24%; H 4.24%; N 6.93%. ESI-MS (m/z). Calculated for $C_{18}H_{16}N_2ZnO_2$ $[M]^{2+}$ 178.02; found 178.02. Calculated for C_6H_7N $[M + H]^+$ 94.07; found 94.07.

Salen Cu(II) complex (8). Brown precipitate (72.6 mg; 19.6% yield). Elemental analysis of $C_{30}H_{30}Cl_2N_4O_{10}Cu{\cdot}3H_2O$ (**8**). Calculated: C 45.32%; H 4.56%; N 7.05%. Found: C 45.05%; H 4.21%; N 6.67%. ESI-MS (m/z). Calculated for $C_{18}H_{16}N_2CuO_2$ $[M]^{2+}$ 177.52; found 177.53. Calculated for C_6H_7N $[M + H]^+$ 94.07; found 94.07.

Salen Pd(II) complex (9). The aldehyde **B** (263.8 mg; 1 mmol) was dissolved in ethanol and a minimum amount of water. Pure ethylenediamine (33.4 µL; 0.5 mmol) was added and stirred at room temperature for 30 minutes, prior to the addition of $Pd(CH_3CO_2)_2$ (112.5 mg; 0.5 mmol), previously dissolved in a minimum amount of water. The mixture was allowed to stir at room temperature for 2 hours, before $NaClO_4{\cdot}H_2O$ (70.5 mg; 0.5 mmol) was added. After 2 hours of stirring at room temperature, the yellowish precipitate was recovered under reduced pressure and washed as usual (85.4 mg; 21.8% yield). ^{1}H NMR (300 MHz, DMSO-d_6) δ 8.97 (d, 2H), 8.20 (d, J = 4.8 Hz, 1H), 7.98 (d, J = 6.3 Hz, 2H), 7.60 (d, J = 2.4 Hz, 1H), 7.46 (dd, J = 8.8, 2.4 Hz, 1H), 6.88 (dd, J = 8.9, 2.4 Hz, 1H), 5.63 (s, 2H), 3.87 (s, 2H), 2.59 (s, 3H). Elemental analysis of $C_{30}H_{30}Cl_3N_4O_{14}Pd{\cdot}H_2O$ (**9**). Calculated: C 39.98%; H 3.58%; N 6.22%. Found: C 39.76%; H 3.98%; N 6.88%. ESI-MS (m/z). Calculated for $C_{18}H_{16}N_2PdO_2$ $[M]^{2+}$ 199.01; found 199.01. Calculated for C_6H_7N $[M + H]^+$ 94.07; found 94.08.

Salnaphen Ni(II) complex (10). Brilliant red solid (233.8 mg; 56% yield). ^{1}H NMR (300 MHz, DMSO-d_6) δ 9.90 (s, 1H), 9.00 (d, J = 6.4 Hz, 2H), 8.62 (s, 1H), 8.03 (d, J = 6.2 Hz, 2H), 7.92 (dt, J = 6.6, 3.3 Hz, 1H), 7.70 (d, J = 2.5 Hz, 1H), 7.59 (dt, J = 6.2, 3.4 Hz, 1H), 7.50 (dd, J = 8.9, 2.4 Hz, 1H), 6.93 (d, J = 8.8 Hz, 1H), 5.70 (s, 2H), 2.62 (s, 3H). Elemental analysis of $C_{38}H_{32}Cl_2N_4O_{10}Ni{\cdot}3H_2O$ (**10**). Calculated: C 51.38%; H 4.31%; N 6.31%. Found: C 51.51%; H 3.92%; N 6.44%. ESI-MS (m/z). Calculated for $C_{26}H_{18}N_2NiO_2$ $[M]^{2+}$ 224.04; found 224.03. Calculated for C_6H_7N $[M + H]^+$ 94.07; found 94.08.

Salnaphen Zn(II) complex (11). Strongly yellow solid (161.7 mg; 38.5% yield). ^{1}H NMR (300 MHz, DMSO-d_6) δ 9.10 (s, 1H), 9.00 (d, J = 6.2 Hz, 2H), 8.32 (s, 1H), 8.00 (d, J = 6.3 Hz, 2H), 7.94 (dt, J = 7.2, 3.7 Hz, 1H), 7.64 (d, J = 2.5 Hz, 1H), 7.54 (dt, J = 8.4, 4.1 Hz, 1H), 7.42 (dd, J = 8.9, 2.5 Hz, 1H), 6.75 (d, J = 8.9 Hz, 1H), 5.64 (s, 2H), 2.60 (s, 3H). Elemental analysis of $C_{38}H_{32}Cl_2N_4O_{10}Zn{\cdot}H_2O$ (**11**). Calculated: C 53.13%; H 3.99%; N 6.52%. Found: C 53.10%; H 4.02%; N 6.55%. ESI-MS (m/z). Calculated for $C_{26}H_{18}N_2ZnO_2$ $[M]^{2+}$ 227.03; found 227.03. Calculated for C_6H_7N $[M + H]^+$ 94.07; found 94.08.

Salnaphen Cu(II) complex (12). Green solid (211.3 mg; 50.4% yield). Elemental analysis of $C_{38}H_{32}Cl_2N_4O_{10}Ni{\cdot}4H_2O$ (**12**). Calculated: C 50.09%; H 4.42%; N 6.15%. Found: C 50.20%; H 3.95%; N 6.31%. ESI-MS (m/z). Calculated for $(C_{38}H_{32}N_4O_2Cu)_2(ClO_4)_2$ $[M]^{2+}$ 739.13; found 739.13.

DNA-binding in solution

General. All solution studies were carried out using freshly prepared solutions of metal complexes. Lyophilized calf thymus (ctDNA) was purchased from Sigma Aldrich and resuspended in 1.0 M Tris-HCl pH 7.5 to be used as a model of the double-stranded **B** conformation of DNA. The final DNA concentration was assessed by measuring the absorbance at 260 nm by UV spectrophotometry and using 6600 M^{-1} cm^{-1} as the molar extinction coefficient. G4 oligonucleotide sequences were purchased from Sigma-Aldrich and IDT (Integrated DNA Technologies) in HPLC purity grade and are reported in Table S1.† Oligonucleotides were resuspended in 50 mM Tris-HCl and 100 mM KCl, pH 7.5 to give 100 µM stock solutions. G4 sequences were allowed to fold into G4 structures by heating the solutions up to 90 °C for 5 min prior to slowly cooling down to room temperature overnight. All experiments were carried out in 50 mM Tris-HCl and 100 mM KCl at pH 7.5.

UV-visible absorption. UV-vis spectra were recorded at room temperature on a double-beam Cary 100 Scan spectrophotometer (Varian Inc.), from 200 nm to 700 nm. Titrations were carried out by increasing the addition of DNA to a constant concentration of the metal complex (previously determined to reach an absorbance of 0.4 at the characteristic wavelength peak). To avoid the dilution of the metal complex during titration, for each addition of DNA solution, the same volume of double concentrated metal complex solution was added to the experimental beam. Measurements were made 2 min after each addition to the reaction mixture, to ensure the complete formation of the intermolecular complex. Binding constants Kb of the double-stranded and quadruplexes DNA with the complex were determined by non-linear fitting of the titration results, thanks to the equation described in the literature, on the supramolecular.org website.[51]

Circular dichroism. CD experiments were performed on a Jasco J-715 spectropolarimeter at room temperature, with the following parameters: range 600–220 nm; step resolution 1.0 nm; speed 200 nm min^{-1}; response 0.5 s; accumulation 4. Fifty μM ctDNA or 1 μM of each quadruplex sequence was titrated with increasing amounts of the metal complex. To ensure that DNA concentration remained unaltered over the experiment, for each addition of the metal complex solution, the same volume of double concentrated DNA solution was added. Measurements were performed 2 min after each addition to the reaction mixture, to ensure the complete formation of intermolecular complexes.

FRET melting assay. FRET experiments were conducted on an Applied Biosystems™ QuantStudio 6 PCR cycler equipped with a FAM filter. For the FRET experiments, the same sequences as those for the UV-vis and CD assays were used, as reported in Table S1,† with FAM and TAMRA probes. The **B** conformation of DNA was mimicked by the sequence 5′ – TATAGCTA/iSp18/TATAGCTATA – 3′ (where iSp18 = [(–CH_2–CH_2–O–)$_6$]), named dsDNA. Lyophilized oligonucleotides were resuspended in 1 mM Tris-HCl and diluted in 60 mM (dsDNA, hTelo, cKIT-1, cKIT-2, cKIT-SP, kRAS, BCL2) or 10 mM (cMYC, RET) potassium cacodylate buffer, pH 7.2, before their folding into G4 or double-stranded structures through the same procedure as described previously. All fluoro-labelled oligonucleotides were used at a final concentration of 0.2 μM. Metal complexes were freshly resuspended in DMSO and used at a final concentration of 1 μM, to reach a DNA : drug ratio equal to 1 : 5. DMSO never exceeded 0.1% of the final volume. Finally, FAM emission was acquired from 25 °C to 95 °C, with a stepwise increase of 1 °C every 30 s. Data were normalized from 0 to 1, and measurements were made in duplicate. The melting temperature of the G4 oligonucleotides in the presence of the metal complex was compared to the melting temperature of the G4 oligonucleotide alone, to give ΔT_M. Also, the evolution of the stabilizer behaviour of **1**, **6** or **10** towards G4 oligonucleotides (0.2 μM) was also monitored in a FRET melting competitive assay, with increasing amounts of non-fluorescent ctDNA.

Molecular dynamics simulations. Equilibrium molecular dynamics simulation was performed considering the Ni-salphen **1** and Ni-salnaphen **10** complexes interacting with either the human *kRAS* or *BCL2* promoters. The starting structures of the two G4 have been retrieved from the protein data bank pdb codes 6T51[59] and 6ZX7,[60] respectively. To assess the formation of stable aggregates the two metal complexes have been placed in a water box together with the chosen G4 and the formation of the interaction has been spontaneously observed through equilibrium MD simulations. Cl^- ions have been added to the water box to ensure electroneutrality. The amber force field including the bsc1 correction[61] was used to model DNA, while water has been described by the TIP3P model.[62] The force fields of the two metal complexes have been parameterized following the generalized amber force field (GAFF) approach. The point charges have been obtained by fitting the restrained electrostatic potential (RESP) following the gaff protocol. To assist the parameterization of the force field the MCPB.py[63] utility has been used. All the MD simulations have been performed in the isothermal and isobaric ensemble, with temperature and pressure conservation being enforced using a Langevin thermostat and barostat. A time step of 4 fs has been used to numerically solve the Newton equation of motion thanks to the simultaneous use of Rattle and Shake and Hydrogen Mass Repartition (HMR) approach.[64] All the simulations have been performed using NAMD[65,66] and analysed and visualized by VMD.[67]

Biological activity

Cell culture. Malignant pancreatic T3M4, hormone-dependent breast T47D and triple-negative MDA-MB-231 breast cancer cell lines were obtained from the American Type Culture Collection (ATCC) (Rockville, MD, USA). Cell lines were maintained as monolayers in red phenol-free RPMI-1640 culture medium, supplemented with 10% heat inactivated fetal bovine serum (FBS), 2 mM L-glutamine, and 0.1% penicillin/streptomycin. Estradiol (10 nM) was also added to the T47D cell culture medium. When reaching an 80–90% confluence, the cells were sub-cultured using trypsin 0.1% – EDTA. The cells were grown under a humidified atmosphere, with 5% CO_2, at 37 °C. FBS was purchased from Biowest, while RPMI-1640 medium, L-glutamine, penicillin/streptomycin and trypsin-EDTA were purchased from Sigma Aldrich.

Immunocytofluorescence. T3M4 cells (4.0×10^4) were grown on glass coverslips in 35 mm culture plates, and allowed to attach for 24 hours, before treatment with 5, 10 or 50 μM of the considered compound for 24 hours. Cells were fixed with cold methanol/acid acetic (3 : 1) for 10 min, at −20 °C. After PBS 1× washes, blocking was performed using 3% BSA in PBS 1× at RT for 1 h, before incubation with a mouse anti DNA/RNA G-quadruplex antibody BG4 (Absolute Antibody, Ab00174-1.1) diluted 1 : 300 in the blocking solution, for 2 hours at RT. Cells were incubated with an anti-mouse Alexa Fluor™ 594-conjugated antibody (Invitrogen, A11032), diluted 1 : 2500 in PBS 1×, for 1 hour at RT. Nuclei were stained with Hoechst 33 342 (Invitrogen) 1 : 10 000 in PBS 1× for 5 min at RT. Coverslips were mounted with the FluorSave™ reagent (Millipore). After each step, cells were washed 3 times with PBS

1×, for 5 min each. Images were recorded on a hybrid fluorescence microscope (Revolve, ECHO). Nuclear focus quantification was established through biologically independent triplicate tests, where BG4-nuclear foci were detected and counted by automated focus detection/quantification from 100 nuclei under each condition using FiJI software macro FindFoci.[68]

RNA preparation. 1.2×10^5 T3M4 cells and 2.0×10^5 T47D cells were seeded in 60 mm culture plates. After 48 hours, the cells were incubated with either the vehicle (0.2% DMSO) or 50 μM of the metal complex for 6 and 24 hours. Total RNAs were extracted and purified using the ReliaPrep™ RNA Cell Miniprep System (Promega), following the manufacturer's instructions. Concentration of isolated nucleic acids were determined by measuring the absorbance at 260 nm, and purity was assessed by measuring the absorbance at 230 nm and 280 nm on a Nanodrop 2000c spectrophotometer. Total RNA (1 μg) was reverse transcribed into cDNA using the OneScript Plus cDNA Synthesis kit (ABM), according to the manufacturer's instructions.

Primer design. qPCR primers were designed using the Human – Ensembl website, and IDT Oligo Analyzer. All primers were tested, and parameters were optimized before utilization. Primer sequences and the corresponding conditions are listed in Table S4.†

RT-qPCR. Quantitative real time polymerase chain reaction assays were performed using 1× Takyon™ No Rox SYBR® MasterMix dTTP Blue kit (Eurogentec), and 300 nM of each forward and reverse primers. Reaction mixtures were incubated in a C1000 Touch Real Time PCR Detection System thermocycler (Bio-Rad) with the following cycle conditions: 95 °C for 3 min, followed by 39 cycles of 95 °C for 15 s, primer hybridization temperature for 20 s, 72 °C for 30 s. A final step of 5 s at 55 °C was performed. Relative level of each transcript was calculated using the equation:[69] $(E^{\Delta Ct})_{target}/(E^{\Delta Ct})_{housekeeping}$, where the PCR reaction efficiency $E = 10^{1/-Slope}$, and $\Delta Ct = Ct_{vehicle} - Ct_{treated}$. Normalization was made with the *UBB*, *RPL13A* and *TBP* housekeeping genes.

IC_{50} determination. Cells were seeded in a 96-well plate (T3M4 1.3×10^3 cells per well; MDA-MB-231 4×10^3 cells per well; T47D 2.15×10^3 cells per well) and allowed to attach for 24 hours. Cells were treated with increasing concentrations of the metal complex, or DMSO for control during 48 h. To evaluate the effect of the G4 stabilizers on viability, cells were stained with crystal violet. Absorbance was measured at 595 nm, and the viability of treated cells, relatively to the control group, was calculated by the following equation: $\text{Relative Viability}\,(\%) = \frac{\text{sample absorbance}}{\text{control absorbance}} \times 100.$ The obtained relative viability was plotted against the decimal logarithm of the molecule concentration log([molecule]). The IC_{50} was determined using a non-linear regression on GraphPad Prism 8 software.

Proliferation assays. Cells were seeded in a 24-well plate (T3M4 8×10^3 cells per well; MDA-MB-231 2.5×10^4 cells per well; T47D 1.35×10^4 cells per well), and allowed to attach for 24 hours, prior to treatment. The cells were treated with 1, 10 or 50 μM of the metal complex. A control condition with 0.2% DMSO has always been included. To evaluate the effect of the G4 stabilizers on the proliferation, cell density was measured using a real-time cell imaging system Cytonote (CytonoteScan, Iprasense®). Data were acquired every 24 hours, over 72 hours of treatment.

Statistical analysis. All experiments were performed in at least three biologically independent replicates. Statistical analyses are specified in the legend of each figure and were performed using the GraphPad Prism 8 software. Values with a *p*-value lower than 0.05 were considered as statistically significant. $*p < 0.05$, $**p < 0.01$, $***p < 0.001$, $****p < 0.0001$.

Conclusions

The designed and synthesized transition metal complexes are strong G4 stabilizers. CD and optical spectroscopy measurements in solution highlight their stabilization of specific G4 present in relevant oncogene promoters. Stabilization is considerably more pronounced for G4 than for double-stranded DNA. Moreover, the metal centre plays a pivotal role in modulating the affinity and stabilization of the nucleic acid folding. In particular, the stabilizing effect of Ni(II) compounds **1**, **6** and **10** is on the average larger than that of the other considered metal complexes. In parallel, the size increase of the π-conjugated moiety on the N–N bridge enhances the stabilization of the G4 tetrads. In fact, the G4 stabilization strength is always in the order salnaphen > salphen > salen complexes. These results, confirmed by molecular modelling, highlight the establishment of a persistent binding between G4 and the considered metal complexes, in particular **1** and **10**. Both computational simulations and experimental measurements, in particular the CD spectra, show that the G4-binding of the metal complexes does not induce noticeable structural deformations of the nucleic acid conformation, while it involves an interplay between binding with tetrads and loops.

Tested on different cell lines, all metal complexes show rather limited cytotoxicity, witnessed by the high IC_{50} values, although partial inhibition of cell proliferation has been evidenced. On the other hand, Ni(II) compounds **1**, **6** and **10** induce an increase in the number of nuclear G4s in the treated cell lines. This effect is dose-dependent and may be associated with their capacity to modulate the G4 landscape at the cellular level. Going a step further, the modulation of such structures can be associated with the downregulation of the tested oncogenes. However, despite G4 stabilization by the considered metal compounds, which has been proven in solution and in cells, we cannot exclude other targets that exist in the complex intracellular system. Moreover, the synthesized metal compounds may also play roles unrelated to oncogene downregulation. Considering that G4 can influence several cellular processes, including DNA replication, the induction of G4 structure stabilization by our molecules could also lead to a decrease in cell proliferation, without direct influence on oncogene regulation. Although in the absence of an absolute one-

to-one correspondence between differential G4 stabilization and downregulation of oncogenes, our results prove that the use of metal complexes is beneficial for modulating gene expression. Furthermore, some specific selectivity can be achieved by targeting some genes of interest, *e.g.* the Pt(II) salphen compound **5** with *BCL2* and Pd(II) salen compound **9** with *RET*. Such properties, accompanied by the low observed cytotoxicity, are important in reducing secondary effects of the possible treatments. Overall, our results suggest that the modulation of the equilibrium between the interaction with the loops and/or with the tetrad could be a factor to be exploited for a rational drug design aimed at increasing G4 selectivity.

Author contributions

Aurane Froux: Investigation, methodology, formal analysis, visualization, writing – original draft, and review & editing. Luisa D'Anna: *in silico* investigation and formal analysis. Aurianne Rainot: *in silico* investigation and formal analysis. Camille Neybecker: *in cellulo* investigation and methodology. Angelo Spinello: methodology and review & editing. Riccardo Bonsignore: Methodology and review & editing. Raphaël Rouget: Investigation and methodology. Guillaume Harlé: Methodology and review & editing. Alessio Terenzi: Conceptualization, methodology, formal analysis, writing – original draft, and review & editing. Antonio Monari: Conceptualization, methodology, formal analysis, writing – original draft, and review & editing. Stéphanie Grandemange: Conceptualization; methodology, formal analysis, writing – original draft, review & editing, and supervision. Giampaolo Barone: Conceptualization; methodology, formal analysis, writing – original draft, review & editing, and supervision.

Data availability

- Fitting of the UV-visible spectroscopic data has been performed using the freely available software provided at the following link: **https://app.supramolecular.org/bindfit/**.

- Molecular dynamics simulations have been performed using the NAMD free software (**https://www.ks.uiuc.edu/Research/namd/**) and the data were analysed and visualized using VMD free software (**https://www.ks.uiuc.edu/Research/vmd/**).

- Immunocytofluorescence analysis has been carried out using the freely available Fiji software (**https://imagej.net/software/fiji/**).

- Chemical structures have been drawn using the ChemDraw software (**https://revvitysignals.com/products/research/chemdraw**).

- Plots of spectral measurements have been produced using the GraphPad Prism software (**https://www.graphpad.com/features**).

- NMR spectra have been analyzed using TopSpin Bruker NMR software (**https://www.bruker.com/it/products-and-solutions/mr/nmr-software/topspin.html**).

Conflicts of interest

There are no conflicts to declare.

Acknowledgements

All authors thank GENCI and Explor computing centers and the Platform P3MB for computational resources, as well as ANR and CGI for financial support of this work through Labex SEAM ANR 11 LABEX 086, ANR 11 IDEX 05 02. The authors thank Prof A. Palumbo Piccionello, University of Palermo, for his support with mass spectrometry, and Prof C. Kowol and Dr W. Kandioller, University of Vienna, and Dr Y. Bernhard, L2CM - UMR CNRS 7053, University of Lorraine, for their support with elemental analysis. FRET experiments were performed at the AteN Center of the University of Palermo. The support of the IdEx "Université Paris 2019" ANR-18-IDEX-0001 is also acknowledged. AR is thankful for the co-founding of her Ph.D. program by the Labex Seam of Université Paris Cité and by the University of Palermo. The financial support of the European Union – NextGenerationEU through the Italian Ministry of University and Research under PNRR – M4C2-I1.3 Project PE_00000019 "HEAL ITALIA" CUP (B73C22001250006) is gratefully acknowledged.

References

1 D. Varshney, J. Spiegel, K. Zyner, D. Tannahill and S. Balasubramanian, The regulation and functions of DNA and RNA G-quadruplexes, *Nat. Rev. Mol. Cell Biol.*, 2020, **21**(8), 459–474, DOI: **10.1038/s41580-020-0236-x**.

2 Y. Wang, J. Yang, A. T. Wild, *et al.*, G-quadruplex DNA drives genomic instability and represents a targetable molecular abnormality in ATRX-deficient malignant glioma, *Nat. Commun.*, 2019, **10**(1), 943, DOI: **10.1038/s41467-019-08905-8**.

3 R. Hänsel-Hertsch, A. Simeone, A. Shea, *et al.*, Landscape of G-quadruplex DNA structural regions in breast cancer, *Nat. Genet.*, 2020, **52**(9), 878–883, DOI: **10.1038/s41588-020-0672-8**.

4 N. Kosiol, S. Juranek, P. Brossart, A. Heine and K. Paeschke, G-quadruplexes: a promising target for cancer therapy, *Mol. Cancer*, 2021, **20**(1), 40, DOI: **10.1186/s12943-021-01328-4**.

5 G. Liu, W. Du, X. Sang, *et al.*, RNA G-quadruplex in TMPRSS2 reduces SARS-CoV-2 infection, *Nat. Commun.*, 2022, **13**(1), 1444, DOI: **10.1038/s41467-022-29135-5**.

6 E. Ruggiero and S. N. Richter, Targeting G-quadruplexes to achieve antiviral activity, *Bioorg. Med. Chem. Lett.*, 2023, **79**, 129085, DOI: **10.1016/j.bmcl.2022.129085**.

7 L. D'Anna, T. Miclot, E. Bignon, *et al.*, Resolving a guanine-quadruplex structure in the SARS-CoV-2 genome through circular dichroism and multiscale molecular modeling, *Chem. Sci.*, 2023, **14**(41), 11332–11339, DOI: **10.1039/D3SC04004F**.

8 T. Miclot, C. Hognon, E. Bignon, *et al.*, Structure and Dynamics of RNA Guanine Quadruplexes in SARS-CoV-2 Genome. Original Strategies against Emerging Viruses, *J. Phys. Chem. Lett.*, 2021, **12**(42), 10277–10283, DOI: **10.1021/acs.jpclett.1c03071**.

9 T. Tian, Y. Q. Chen, S. R. Wang and X. Zhou, G-Quadruplex,: A Regulator of Gene Expression and Its Chemical Targeting, *Chem*, 2018, **4**(6), 1314–1344, DOI: **10.1016/j.chempr.2018.02.014**.

10 J. Spiegel, S. Adhikari and S. Balasubramanian, The Structure and Function of DNA G-Quadruplexes, *Trends Chem.*, 2020, **2**(2), 123–136, DOI: **10.1016/j.trechm.2019.07.002**.

11 E. Puig Lombardi and A. Londoño-Vallejo, A guide to computational methods for G-quadruplex prediction, *Nucleic Acids Res.*, 2020, **48**(3), 1603, DOI: **10.1093/nar/gkaa033**.

12 V. Brázda, J. Kolomazník, J. Lýsek, *et al.*, G4Hunter web application: a web server for G-quadruplex prediction, *Bioinformatics*, 2019, **35**(18), 3493–3495, DOI: **10.1093/bioinformatics/btz087**.

13 M. Barshai, B. Engel, I. Haim, Y. Orenstein and F. M. Fadlelmola, G4mismatch: Deep neural networks to predict G-quadruplex propensity based on G4-seq data, *PLoS Comput. Biol.*, 2023, **19**(3), e1010948, DOI: **10.1371/journal.pcbi.1010948**.

14 N. H. Campbell, N. H. A. Karim, G. N. Parkinson, *et al.*, Molecular Basis of Structure–Activity Relationships between Salphen Metal Complexes and Human Telomeric DNA Quadruplexes, *J. Med. Chem.*, 2012, **55**(1), 209–222, DOI: **10.1021/jm201140v**.

15 N. Alegret, J. A. Valdez, A. Rodríguez-Fortea, *et al.*, HMGB1 binds to KRAS promoter G-quadruplex: a new player in oncogene transcriptional regulation?, *Chem. Commun.*, 2016, **52**(1), 64–67, DOI: **10.1039/x0xx00000x**.

16 J. G. Keller, K. M. Hymøller, M. E. Thorsager, *et al.*, Topoisomerase 1 inhibits *MYC* promoter activity by inducing G-quadruplex formation, *Nucleic Acids Res.*, 2022, **50**(11), 6332–6342, DOI: **10.1093/nar/gkac482**.

17 H. Sun, J. Xiang, Y. Shi, *et al.*, A newly identified G-quadruplex as a potential target regulating Bcl-2 expression, *Biochim. Biophys. Acta, Gen. Subj.*, 2014, **1840**(10), 3052–3057, DOI: **10.1016/j.bbagen.2014.07.014**.

18 M. Falabella, J. E. Kolesar, C. Wallace, *et al.*, G-quadruplex dynamics contribute to regulation of mitochondrial gene expression, *Sci. Rep.*, 2019, **9**(1), 5605, DOI: **10.1038/s41598-019-41464-y**.

19 J. Jana, S. Mondal, P. Bhattacharjee, *et al.*, Chelerythrine down regulates expression of VEGFA, BCL2 and KRAS by arresting G-Quadruplex structures at their promoter regions, *Sci. Rep.*, 2017, **7**(1), 40706, DOI: **10.1038/srep40706**.

20 A. M. Psaras, R. K. Carty, J. T. Miller, L. N. Tumey and T. A. Brooks, Indoloquinoline-Mediated Targeted Downregulation of KRAS through Selective Stabilization of the Mid-Promoter G-Quadruplex Structure, *Genes*, 2022, **13**(8), 1440, DOI: **10.3390/genes13081440**.

21 M. H. Hu and J. H. Lin, New Dibenzoquinoxalines Inhibit Triple-Negative Breast Cancer Growth by Dual Targeting of Topoisomerase 1 and the *c-MYC* G-Quadruplex, *J. Med. Chem.*, 2021, **64**(10), 6720–6729, DOI: **10.1021/acs.jmedchem.0c02202**.

22 J. Shen, D. Varshney, A. Simeone, *et al.*, Promoter G-quadruplex folding precedes transcription and is controlled by chromatin, *Genome Biol.*, 2021, **22**(1), 143, DOI: **10.1186/s13059-021-02346-7**.

23 E. Bignon, A. Spinello, T. Miclot, *et al.*, Predicting the Three-Dimensional Structure of the c- *KIT* Proto-Oncogene Promoter and the Dynamics of Its Strongly Coupled Guanine Quadruplexes, *J. Phys. Chem. Lett.*, 2023, **14**(20), 4704–4710, DOI: **10.1021/acs.jpclett.3c00765**.

24 C. Ducani, G. Bernardinelli, B. Högberg, B. K. Keppler and A. Terenzi, Interplay of Three G-Quadruplex Units in the *KIT* Promoter, *J. Am. Chem. Soc.*, 2019, **141**(26), 10205–10213, DOI: **10.1021/jacs.8b12753**.

25 M. Ohanian, M. L. Arellano, M. Y. Levy, *et al.*, A Phase 1a/b Dose Escalation Study of the MYC Repressor Apto-253 in Patients with Relapsed or Refractory AML or High-Risk MDS, *Blood*, 2021, **138**(Supplement 1), 3411, DOI: **10.1182/blood-2021-150049**.

26 J. Hilton, K. Gelmon, P. L. Bedard, *et al.*, Results of the phase I CCTG IND.231 trial of CX-5461 in patients with advanced solid tumors enriched for DNA-repair deficiencies, *Nat. Commun.*, 2022, **13**(1), 3607, DOI: **10.1038/s41467-022-31199-2**.

27 I. Alessandrini, M. Recagni, N. Zaffaroni and M. Folini, On the Road to Fight Cancer: The Potential of G-Quadruplex Ligands as Novel Therapeutic Agents, *Int. J. Mol. Sci.*, 2021, **22**(11), 5947, DOI: **10.3390/ijms22115947**.

28 S. Neidle, Quadruplex Nucleic Acids as Novel Therapeutic Targets, *J. Med. Chem.*, 2016, **13**(59), 5987–6011, DOI: **10.1021/acs.jmedchem.5b01835**.

29 A. Lauria, A. Terenzi, R. Bartolotta, *et al.*, Does ligand symmetry play a role in the stabilization of DNA G-quadruplex host-guest complexes?, *Curr. Med. Chem.*, 2014, **23**(21), 2665–2690, DOI: **10.2174/0929867321666140217155156266**.

30 J. Zegers, DNA G-quadruplex-stabilizing metal complexes as anticancer drugs, *J. Biol. Inorg. Chem.*, 2023, **28**, 117–138, DOI: **10.1007/s00775-022-01973-0**.

31 G. Farine, C. Migliore, A. Terenzi, *et al.*, On the G–Quadruplex Binding of a New Class of Nickel(II), Copper (II), and Zinc(II) Salphen–Like Complexes, *Eur. J. Inorg. Chem.*, 2021, **2021**(14), 1332–1336, DOI: **10.1002/ejic.202100067**.

32 L. D'Anna, S. Rubino, C. Pipitone, *et al.*, Salphen metal complexes as potential anticancer agents: interaction profile and selectivity studies toward the three

G-quadruplex units in the KIT promoter, *Dalton Trans.*, 2023, **52**, 2966–2975.

33 R. Bonsignore, E. Trippodo, A. P. Carreca, *et al.*, Novel half Salphen cobalt(III) complexes: synthesis, DNA binding and anticancer studies, *Dalton Trans.*, 2024, **14**(53), 6311–6322, DOI: 10.1039/D4DT00092G.

34 R. Bonsignore, F. Russo, A. Terenzi, *et al.* The interaction of Schiff Base complexes of nickel(II) and zinc(II) with duplex and G-quadruplex DNA, *J. Inorg. Biochem.*, 2018, (178), 106–114.

35 W. Streciwilk, A. Terenzi, R. Misgeld, *et al.* Metal NHC Complexes with Naphthalimide Ligands as DNA-Interacting Antiproliferative Agents, *ChemMedChem*, 2017, (12), 214–225, DOI: 10.1002/cmdc.201600557.

36 W. Streciwilk, A. Terenzi, F. Lo Nardo, *et al.*, Synthesis and Biological Evaluation of Organometallic Complexes Bearing Bis-1,8-naphthalimide Ligands, *Eur. J. Inorg. Chem.*, 2018, 3104–3112, DOI: 10.1002/ejic.201800384.

37 A. Arola and R. Vilar, Stabilisation of G-Quadruplex DNA by Small Molecules, *Curr. Top. Med. Chem.*, 2008, **8**(15), 1405–1415, DOI: 10.2174/156802608786141106.

38 A. Terenzi, D. Lötsch, S. van Schoonhoven, *et al.*, Another step toward DNA selective targeting: Ni II and Cu II complexes of a Schiff base ligand able to bind gene promoter G-quadruplexes, *Dalton Trans.*, 2016, **45**(18), 7758–7767, DOI: 10.1039/C6DT00648E.

39 A. Terenzi, R. Bonsignore, A. Spinello, *et al.*, Selective G-quadruplex stabilizers: Schiff-base metal complexes with anticancer activity, *RSC Adv.*, 2014, (63), 33245–33256, DOI: 10.1039/C4RA05355A.

40 G. Barone, N. Gambino, A. Ruggirello, A. Silvestri, A. Terenzi and V. T. Liveri, Spectroscopic study of the interaction of NiII-5-triethyl ammonium methyl salicylidene ortho-phenylendiiminate with native DNA, *J. Inorg. Biochem.*, 2009, **103**(5), 731–737, DOI: 10.1016/j.jinorgbio.2009.01.006.

41 A. W. Kleij, D. M. Tooke, A. L. Spek and J. N. H. Reek, A Convenient Synthetic Route for the Preparation of Nonsymmetric Metallo-salphen Complexes, *Eur. J. Inorg. Chem.*, 2005, 4626–4634, DOI: 10.1002/ejic.200500628.

42 A. Ambrus, D. Chen, J. Dai, T. Bialis, R. A. Jones and D. Yang, Human telomeric sequence forms a hybrid-type intramolecular G-quadruplex structure with mixed parallel/antiparallel strands in potassium solution, *Nucleic Acids Res.*, 2006, **34**(9), 2723–2735, DOI: 10.1093/nar/gkl348.

43 J. Dai, C. Punchihewa, A. Ambrus, D. Chen, R. A. Jones and D. Yang, Structure of the intramolecular human telomeric G-quadruplex in potassium solution: a novel adenine triple formation, *Nucleic Acids Res.*, 2007, **35**(7), 2440–2450, DOI: 10.1093/nar/gkm009.

44 J. Dai, D. Chen, R. A. Jones, L. H. Hurley and D. Yang, NMR solution structure of the major G-quadruplex structure formed in the human BCL2 promoter region, *Nucleic Acids Res.*, 2006, **34**(18), 5133–5144, DOI: 10.1093/nar/gkl610.

45 S. Cogoi and L. E. Xodo, G-quadruplex formation within the promoter of the KRAS proto-oncogene and its effect on transcription, *Nucleic Acids Res.*, 2006, **34**(9), 2536–2549, DOI: 10.1093/nar/gkl286.

46 A. Ambrus, D. Chen, J. Dai, R. A. Jones and D. Yang, Solution structure of the biologically relevant G-quadruplex element in the human c-MYC promoter. Implications for G-quadruplex stabilization, *Biochemistry*, 2005, **44**(6), 2048–2058, DOI: 10.1021/bi048242p.

47 X. Tong, W. Lan, X. Zhang, H. Wu, M. Liu and C. Cao, Solution structure of all parallel G-quadruplex formed by the oncogene RET promoter sequence, *Nucleic Acids Res.*, 2011, **39**(15), 6753–6763, DOI: 10.1093/nar/gkr233.

48 A. Kotar, R. Rigo, C. Sissi and J. Plavec, Two-quartet kit* G-quadruplex is formed via double-stranded pre-folded structure, *Nucleic Acids Res.*, 2018, **47**, 2641–2653, DOI: 10.1093/nar/gky1269.

49 V. Butera, L. D'Anna, S. Rubino, *et al.*, How the Metal Ion Affects the ^{1}H NMR Chemical Shift Values of Schiff Base Metal Complexes: Rationalization by DFT Calculations, *J. Phys. Chem. A*, 2023, **127**(44), 9283–9290, DOI: 10.1021/acs.jpca.3c05653.

50 A. De Rache and J. L. Mergny, Assessment of selectivity of G-quadruplex ligands via an optimised FRET melting assay, *Biochimie*, 2015, **115**, 194–202, DOI: 10.1016/j.biochi.2015.06.002.

51 D. Brynn Hibbert and P. Thordarson, The death of the Job plot, transparency, open science and online tools, uncertainty estimation methods and other developments in supramolecular chemistry data analysis, *Chem. Commun.*, 2016, **52**(87), 12792–12805, DOI: 10.1039/C6CC03888C.

52 T. A. Brooks, S. Kendrick and L. Hurley, Making sense of G-quadruplex and i-motif functions in oncogene promoters: G-quadruplex and i-motif in oncogene promoters, *FEBS J.*, 2010, **277**(17), 3459–3469, DOI: 10.1111/j.1742-4658.2010.07759.x.

53 S. Cogoi, V. Rapozzi, S. Cauci and L. E. Xodo, Critical role of hnRNP A1 in activating KRAS transcription in pancreatic cancer cells: A molecular mechanism involving G4 DNA, *Biochim. Biophys. Acta, Gen. Subj.*, 2017, **1861**(5), 1389–1398, DOI: 10.1016/j.bbagen.2016.11.031.

54 W. Wang, S. Hu, Y. Gu, *et al.*, Human MYC G-quadruplex: From discovery to a cancer therapeutic target, *Biochim. Biophys. Acta, Rev. Cancer*, 2020, **1874**(2), 188410, DOI: 10.1016/j.bbcan.2020.188410.

55 G. Biffi, D. Tannahill, J. McCafferty and S. Balasubramanian, Quantitative visualization of DNA G-quadruplex structures in human cells, *Nat. Chem.*, 2013, **5**(3), 182–186, DOI: 10.1038/nchem.1548.

56 A. De Magis, M. Kastl, P. Brossart, A. Heine and K. Paeschke, BG-flow, a new flow cytometry tool for G-quadruplex quantification in fixed cells, *BMC Biol.*, 2021, **19**(1), 45, DOI: 10.1186/s12915-021-00986-6.

57 S. J. Angyal, P. J. Morris, J. R. Tetaz and J. G. Wilson, The Sommelet reaction. Part III. The choice of solvent and the effect of substituents, *J. Chem. Soc.*, 1950, 2141–2145.

58 W. Kandioller, J. Theiner, B. K. Keppler and C. R. Kowol, Elemental analysis: an important purity control but prone

to manipulations, *Inorg. Chem. Front.*, 2022, **9**(3), 412–416, DOI: **10.1039/D1QI01379C**.

59 J. Marquevielle, M. V. Vasantha Kumar, J. L. Mergny and G. F. Salgado, 1H, 13C, and 15N chemical shift assignments of a G-quadruplex forming sequence within the KRAS proto-oncogene promoter region, *Biomol. NMR Assignments*, 2018, **12**, 123–127, DOI: **10.1007/s12104-017-9793-0**.

60 S. Bielskutė, J. Plavec and P. Podbevšek, Oxidative lesions modulate G-quadruplex stability and structure in the human BCL2 promoter, *Nucleic Acids Res.*, 2021, **49**(4), 2346–2356, DOI: **10.1093/nar/gkab057**.

61 R. Galindo-Murillo, J. C. Robertson, M. Zgarbová, *et al.*, Assessing the Current State of Amber Force Field Modifications for DNA, *J. Chem. Theory Comput.*, 2016, **12**(8), 4114–4127, DOI: **10.1021/acs.jctc.6b00186**.

62 P. Mark and L. Nilsson, Structure and Dynamics of the TIP3P, SPC, and SPC/E Water Models at 298 K, *J. Phys. Chem. A*, 2001, **105**(43), 9954–9960, DOI: **10.1021/jp003020w**.

63 P. Li and K. M. Merz, MCPB.py: A Python Based Metal Center Parameter Builder, *J. Chem. Inf. Model.*, 2016, **56**(4), 599–604, DOI: **10.1021/acs.jcim.5b00674**.

64 C. W. Hopkins, S. Le Grand, R. C. Walker and A. E. Roitberg, Long-Time-Step Molecular Dynamics through Hydrogen Mass Repartitioning, *J. Chem. Theory Comput.*, 2015, **11**(4), 1864–1874, DOI: **10.1021/ct5010406**.

65 J. C. Phillips, R. Braun, W. Wang, *et al.*, Scalable molecular dynamics with NAMD, *J. Comput. Chem.*, 2005, **26**(16), 1781–1802.

66 J. C. Phillips, D. J. Hardy, J. D. C. Maia, *et al.*, Scalable molecular dynamics on CPU and GPU architectures with NAMD, *J. Chem. Phys.*, 2020, **153**(4), 044130, DOI: **10.1063/5.0014475**.

67 W. Humphrey, A. Dalke and K. Schulten, VMD: visual molecular dynamics, *J. Mol. Graphics*, 1996, **14**(1), 22–28, DOI: **10.1016/0263-7855(96)00018-5**.

68 A. D. Herbert, A. M. Carr, E. Hoffmann and M. Lichten, FindFoci: A Focus Detection Algorithm with Automated Parameter Training That Closely Matches Human Assignments, Reduces Human Inconsistencies and Increases Speed of Analysis, *PLoS One*, 2014, **9**(12), e114749, DOI: **10.1371/journal.pone.0114749**.

69 M. W. Pfaffl, A new mathematical model for relative quantification in real-time RT-PCR, *Nucleic Acids Res.*, 2001, **29**(9), 45e–445, DOI: **10.1093/nar/29.9.e45**.

